In-situ Observation of Point-Defect-Induced Unit-Cell-Wise Energy Storage Pathway in Antiferroelectric $PbZrO_3$

Xian-Kui Wei, Chun-Lin Jia, Krystian Roleder, Rafal E. Dunin-Borkowski, and Joachim Mayer*

Dr. X.-K. Wei, Prof. C.-L. Jia, Prof. R. E. Dunin-Borkowski, Prof. J. Mayer
Ernst Ruska-Centre for Microscopy and Spectroscopy with Electrons, Research Center Jülich, 52425 Jülich, Germany
E-mail: x.wei@fz-juelich.de
Prof. C.-L. Jia
School of Microelectronics, Xi'an Jiaotong University, Xi'an 710049, China
Prof. K. Roleder
Institute of Physics, University of Silesian, 40007 Katowice, Poland
Prof. J. Mayer
Gemeinschaftslabor für Elektronenmikroskopie (GFE) RWTH Aachen, Ahornstraße 55, 52074 Aachen, Germany

Phase transition is established to govern the electrostatic energy storage for antiferroelectric-type dielectric capacitors. However, the source of inducing the phase transition and the pathway of storing the energy remains elusive so far given the ultrafast charging/discharging process under normal working conditions. Here, by slowing down the phase transition speed using electron beam irradiation as an external stimulus, we capture the in-situ dynamic energy storage process in antiferroelectric $PbZrO_3$ by using atomic-resolution transmission electron microscopy. Specifically, we found that oxygen-lead-vacancy-induced defect core acts as a seed to initiate the antiferrodistortive-to-ferrodistortive transition in antiparallel-Pb-based structural frames. Associated with polarity evolution of the compressively strained defect core, the ferroelectric-ferrodistortive state expands bilaterally along *b* axis direction and then develops into charged domain configurations during the energy-storage process, which is further evidenced by observations at the ordinary ferroelectric states. With filling the gap of perception, our findings provide a straightforward approach of unveiling the unit-cell-wise energy storage pathway in chemical defect engineered dielectric ceramics.

1. Introduction

Dielectric capacitors, characteristic of ultrafast charging/discharging rate, high energy-storage density, voltage endurance and good reliability, are receiving a great deal of attention for their potential applications in electronic devices and electrical power systems.[1] Towards further improving the recoverable energy density $U_e = \int EdP$ (**Figure 1**a), two complementary approaches are mainly implemented so far: the macroscopic one by developing novel material design strategies such as polymorphic nanodomain[2] and grain-orientation-engineered multilayers,[3] and the microscopic one by unveiling the energy-stroage pathway and mechanism.[4,5] Obviously, in-situ relealing the energy storage pathway provides a fundamental perspective to elaborate the structure-property relationship. Nevertheless, the ultrafast charging and discharging processes, completed in milliseconds or less, in traditional parallel-plate capacitors (Figure 1b) bring great challenges to capture the transient transition between different phase states.[6-8]

Different from linear and ferroelectric (FE) dielectrics,[2,9] antiferroelectrics (AFEs) such as $PbZrO_3$ offer an appropriate prototype for unveiling the microscopic scale energy storage process given its inherent coupling with the AFE-to-FE phase transition.[10-13] On the one hand, it is reported that the illumination electron beam in transmission electron microscopy (TEM) may act as an external stimulus to slow down the excitation and image the structural phase transition in real time.[14,15] This endows a possibility of probing the storage process of energy through atomic resolution TEM imaging (Figure 1c). On the other hand, the small critical thickness (~6.5 nm) provides a favorable condition for resolving the structural order parameters,[16,17] e.g., tilting of oxygen octahedra,[18,19] and daynamically tracking their evolution during the AFE-to-FE transition. In addition, we find that the remnant polarization (P_r), ranging from about 2.5 to 8.3 μC cm^{-2} in

the polarization-electric field (*P*-*E*) double-hysteresis loop (Figure 1a and Figure S1, Supporting Information), is ubiquitous in pure and doped $PbZrO_3$[12,20-22], $AgNbO_3$ and $NaNbO_3$.[23-25] As a factor of reducing the U_e, the inescapable P_r, irrelevant to antiparallel cation shifts with either complete or partial offset, motivates us to find out its relationship with the ubiquitous structural defects, e.g., point and planar defects.[26-28]

Here, based on excitation of illumination electron beam,[14,29,30] we investigate in-situ the impact of oxygen-lead-vacancy-induced defect structure on phase transitions of $PbZrO_3$ during energy storage in an image-corrected TEM. By simultaneously imaging light oxygen anions and heavy cations using negative spherical-aberration imaging (NCSI) technique,[17,31,32] our time-resolved dynamic study reveals that with retention of antiparallel Pb displacements, the vacancy-driven defect structure triggers an antiferrodistortive-to-ferrodistortive (AFD-to-FD) state transition in a stripe manner with variable width at unit-cell-wise level. Along with vanishing antiparallel Pb displacements, the FE/FD state instantly transforms into ordinary FE states. During the charge storage process, we also found presence and density increase of metastable charged domain walls. Our findings present a unit-cell-scale energy storage pathway, which offers a strategy to expose atomic-scale energy-storage process and structure-property relation in dielectric energy materials.

2. Results and Discussion

It is known that the orthorhombic AFE $PbZrO_3$ (space group *Pbam*) is characteristic of antiparallel Pb shifts along $[100]_O$ direction and antiphase rotations of oxygen octahedra along $[210]_O$ and $[\bar{2}10]_O$ direction ($a^-a^-c^0$ in Glaser's notation).[33,34] As viewed along $[001]_O$ direction, the oxygen atoms therefore undergo $(0 \uparrow 0 \downarrow)$ and $(0 \downarrow 0 \uparrow)$ shift behavior along y/$[010]_O$ direction

and (0 ← 0 →) behavior along x/[100]$_O$ direction (Figure 1d and Figure S2a, Supporting Information). By carrying out thermal annealing treatments, i.e., heating the specimen to a temperature slightly above T_C (≈ 500 K) and then cooling it down to room temperature, oxygen and Pb vacancies are successfully introduced into the lamella specimen (see Experimental Section). Observation of the intrinsic translational boundaries (dark-contrast straight lines in Figure 1e) and the structural modulation feature (Figure 1f) clearly evidence that the AFE phase is well maintained after the thermal treatment, where the lattice parameter ratio is measured as $b_{AF}/2a_{AF}$ = 0.995.

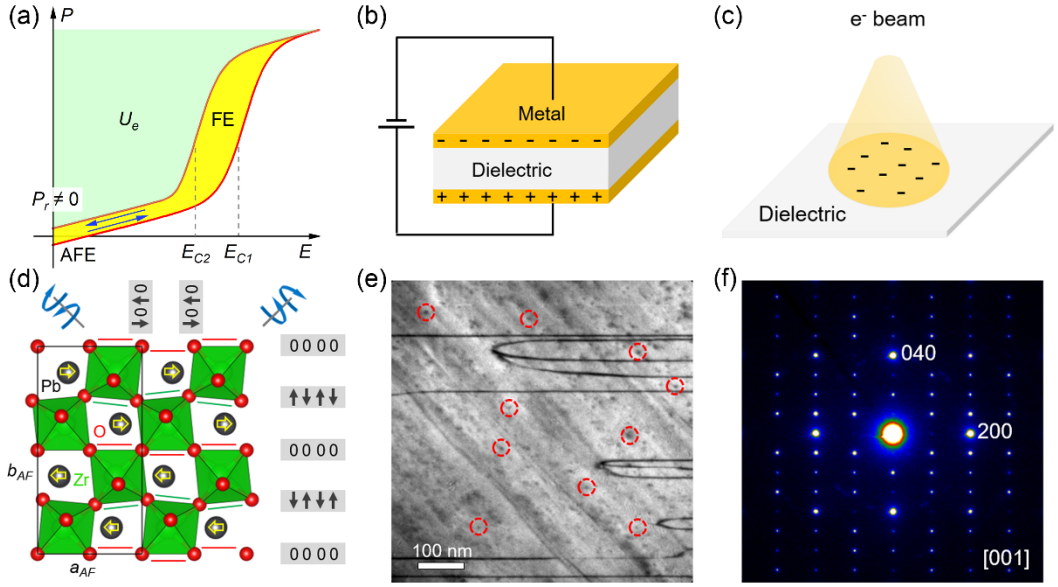

Figure 1. a) Schematic hysteresis loop at $E \geq 0$ with annotation of the recoverable energy-storage density U_e (green area) and coercive fields E_{C1} and E_{C2}. In real situations, the nonzero remnant polarization P_r at E = 0 usually broadens the linear region of the P-E loop. b) Typical capacitor geometry for electric-field biasing experiments. c) Illustration of electron beam illumination as a stimulus for exciting and recording the structural phase transition. d) Crystal structure of AFE $PbZrO_3$ viewed along [001]$_O$ direction. The black arrows and zeros and line segments (red and green) characterize the AFD tilting of oxygen octahedra along the x/[100]$_O$ and y/[010]$_O$ direction,

respectively. The empty yellow arrows denote antiparallel Pb shifts. e) Dark-field TEM image of $PbZrO_3$ recorded along $[001]_O$ with annotation of vacancy induced structural defects (red circles). (f) Corresponding selected area electron diffraction (SAED) pattern taken along $[001]_O$ direction.

In our experiments, a series of atomic-resolution TEM images were recorded from a vacancy-accumulating region using the NCSI technique along $[001]_O$ direction (**Figure 2**a). From a magnified central region of the initial AFE state (t = -5 s), we see that peak intensities of some oxygen columns (yellow dashed circles) are clearly reduced, which are accompanied with contrast enhancement of nearby Pb columns (green dashed squares, Figure 2b). By constructing different structural models, either surface or probability one, our multislice-based image simulations indicate that the oxygen and Pb vacancies, with reduction and increment on peak intensity, tend to locate on surfaces of the specimen (Figure 2c,d and Figure S3, Supporting Information). Through fitting peak positions of atomic columns using a 2D Gaussian function,[35] our mapping reveals a dislocation-free defect core, which is characteristic of vortex-like polar displacements of oxygen against centers of nearest-neighboring Zr columns (Figure 2e). Accordingly, a self-compensated polarization (P_S) configuration is formed inside the defect core, which resembles the topological domain states of $BaTiO_3$ as the FE nanorods are embedded in a $SrTiO_3$ matrix.[36,37]

Apart from breaking the AFD order of oxygen octahedra, we notice that the antiparallel Pb displacements near the defect core are also partially modified (Figure 2f and Figure S4a, Supporting Information). To understand the corresponding structural change, we further analyze local lattice deformation near the defect core using geometric phase analysis (GPA).[38] Referring to a region near the defect core, we see from the e_{xx} map that point vacancies lead to local lattice expansion along $[100]_O$ direction, which compresses the nearby vacancy-free regions (Figure 2g-

i). In sharp contrast, evident lattice deformation was not observed from the e_{yy} map. From the e_{xy} and rot_{xy} maps, we see a dramatic shear strain and lattice rotation near the defect core, which can be attributed to the structural change caused by atomic polar displacements.

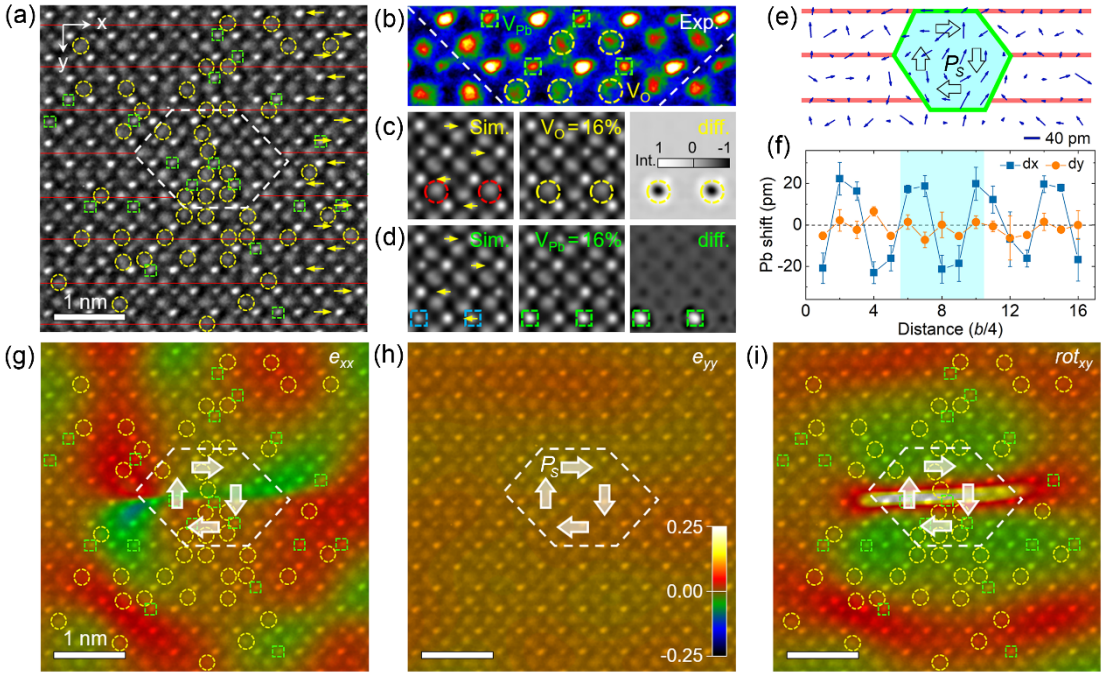

Figure 2. a) Atomic-resolution TEM image of the initial AFE phase (t = -5 s) along $[001]_O$ direction. The white dashed polygon, red solid lines and yellow arrows denote the defect core, centrosymmetric oxygen sites and antiparallel Pb shifts, respectively. b) Enlarged view of the vacancy-containing defect core. c,d) Simulated images of ideal (left panels) and vacancy-containing (middle panels) $PbZrO_3$ structure and their difference (right panels) for specimens with thickness = 10.2 nm and defocus = 8.5 nm. The vacancy concentration at specific columns is V_O = V_{Pb} = 16%. e) Map of oxygen displacements near the defect core. f) Pb shifts along the x//$[100]_O$ and y//$[010]_O$ directions as a function of distance along y direction. g-i) Strain maps of e_{xx}, e_{yy}, lattice rotation (rot_{xy}) and point vacancy distribution overlaid on the TEM images, respectively. The white arrows denote the polarization direction within the defect core.

Starting from the initial AFE state, we see that during irradiation of the electron beam, the self-compensated defect core (~ 2 nm in diameter) evolves into a dynamic polar structure with local destroy of the antiparallel Pb arrangements (**Figure 3**a-d and Figure S4b-d, Supporting Information). Meanwhile, the defect core initiates an AFD-to-FD transition in a stripe region with width of ~b_{AF} along x direction, which is characterized by y-direction transformation of oxygen shifts from $(0 \downarrow 0 \uparrow)/(0 \uparrow 0 \downarrow)$ in the AFD state to $(0 \downarrow \uparrow \uparrow)/(0 \uparrow \downarrow \downarrow)$ in the FD-I state.[14] Herein, the zeros '0' marked by red solid line denote oxygen atoms locating at the centrosymmetric positions. This reveals that polar distortion occurs to the oxygen octahedral in the FD state, which generates a polarization with $P_S \approx 3$ μC cm^{-2} that essentially runs along $[\bar{1}00]_O$ direction according to previous TEM measurement[14] (Figure S2b, Supporting Information). As the irradiation time increases to t = 20 s, the FD-I state expands in unit cell wise along y direction, which is accompanied with dynamic size change of the defect core.

Clearly, the presence of net polarization in the AFE/AFD-to-FE/FD transition is attributed to storage of electrostatic energy from the electron beam. At t = 35 s, the defect core further induces a new FD-II state. With retaining the FD-I state polarization orientation, the FD-II state is characterized by $(0 \downarrow \downarrow \uparrow)/(0 \uparrow \uparrow \downarrow)$ oxygen shifts along y direction (Figure 3e and Figure S5a,b, Supporting Information). Accompanied with the structural transition, the polarization forms a partial offset configuration inside the defect core to lower the local electrostatic energy.[32] More interestingly, through reversing the x-direction shift but not the y-direction shift of oxygen, the FD-I state transforms into a new FD-III state, which corresponds to P_S reversal from $[\bar{1}00]_O$ to $[100]_O$ direction. This reveals that the energy storage is accompanied with formation of charged FD domain walls (Figure 3f,g and Figure S5c, Supporting Information). Under continuous

irradiation of the electron beam, the injected energy dynamically propagates to nearby regions through motion and density increase of the FD domain walls, which lie in $(100)_O$, $(210)_O$ and $(\bar{2}10)_O$ crystal planes and their width is about one octahedral unit.

Besides changes of the structural order parameters, the lattice parameters from the displayed image area are measured as a function of irradiation time. At the AFE state with $t < 0$ s, the average lattice parameters are $a_{AF} \approx 0.5813$ nm, $b_{AF}/2 \approx 0.5914$ nm and thus the lattice ratio is $b_{AF}/2a_{AF} \approx 1.024$. Referring to the value measured from the SAED pattern, these values of local lattice parameters reveal that the point vacancies near the defect core distort the unit cells at nanometer scale. At $t > 0$ s, the a_{AF} axis slightly increases until $t = 40$ s and the b_{AF} axis continuously decreases (Figure 3h). As a result, the ratio is reduced to $b_{AF}/2a_{AF} = 1.022$. Since the P_S of the FD phase is essentially running along x direction,[14] the reduced lattice ratio (at $t > 0$ s) supports the polarization-strain coupling relation[39] and favors the AFD-to-FD transition. Assuming c_{AF} axis is a constant with $c_{AF}/2 = 4.113$ Å, it can be seen that this phase transition leads to expansion of the unit-cell volume at the initial stage, which is 0.26% at the maximum. Around $t \approx 50$ s, we see that the a_{AF} axis decreases and the unit-cell volume is compressed by about -0.24%. This can be attributed to presence of the head-to-head dipole configuration across the nearly 180° charged domain walls in the FD phase,[40] which take a larger proportion in this local region (Fig. 3f,g).

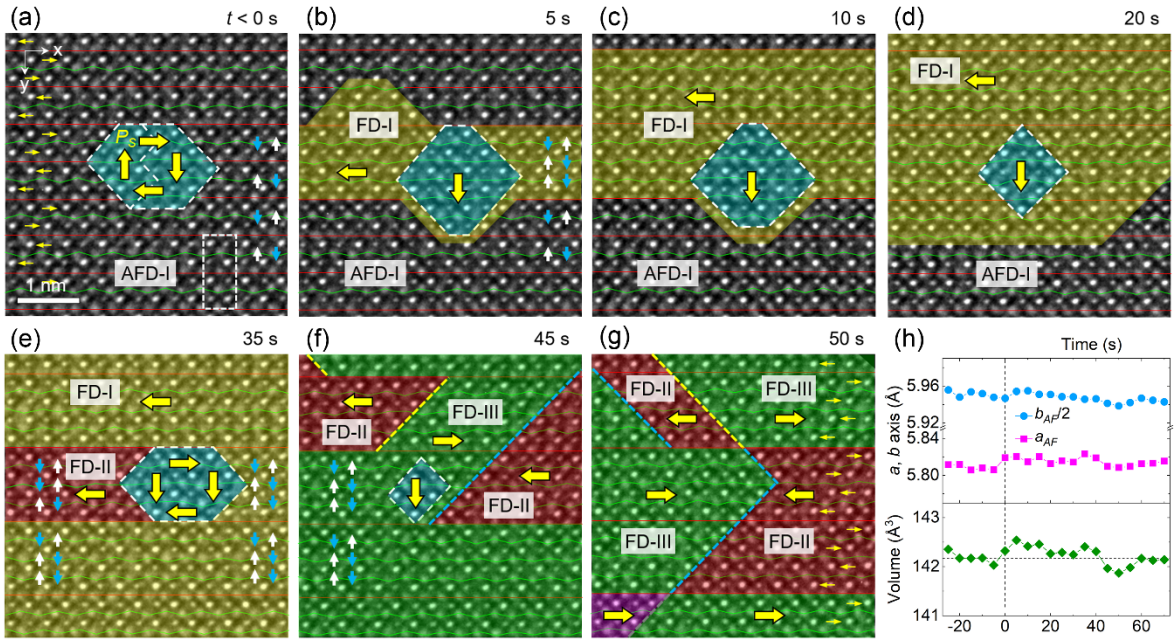

Figure 3. a-g) Evolution of phase and domain structures (yellow, red, green and purple shadows) near the defect core (cyan region) as a function of electron-beam irradiation time. The polarization (P_S, yellow thick arrows) in the FD states and defect core is determined by mapping oxygen shifts against centers of nearest-neighboring Zr columns (see Figure S5, Supporting Information). The (red, green) solid lines and the (white, blue) arrows highlight the characteristic oxygen displacements along y direction. The yellow thin arrows in (a) and (g) denote antiparallel Pb shifts in the AFD and FD states. The white dashed rectangle denote the AFE unit cell. The yellow and blue dashed lines in (f,g) denote the tail-to-tail and head-to-head charged FE domain walls. h) Evolution of lattice parameters and volume ($V = a_{AF} \times b_{AF} \times c_{AF}/4$) as a function of electron-beam irradiation time.

First-principles calculations on $PbZrO_3$ have revealed that the difference in ground-state energy is remarkably small between the FE rhombohedral-like (FE_{RL}) and AFE orthorhombic

phases. Of particular interest is that compressive strain obviously favors formation of the FE_{RL} phase.[41,42] Being consistent with the calculation result, our GPA analysis reveals that the defect core is essentially under a compressively strained condition during the dynamic storage process of energy (**Figure 4**a-f). Besides the time-resolved maps, it can also be seen from the extracted line profiles that the e_{xx} values may go down to -30% at the center of the defect core, while the nearby tensile strain is only in the range of 3 ~ 5% (Figure 4g). This situation remains even when the charged and uncharged FD domain walls were created by the electron-beam irradiation. This indicates that the strain conditions of the defect core (Figures S6 and S7, Supporting Information), governed by distribution and dynamic motion of the point defects, play a decisive role in mediating storage and propagation of the electrostatic energy.

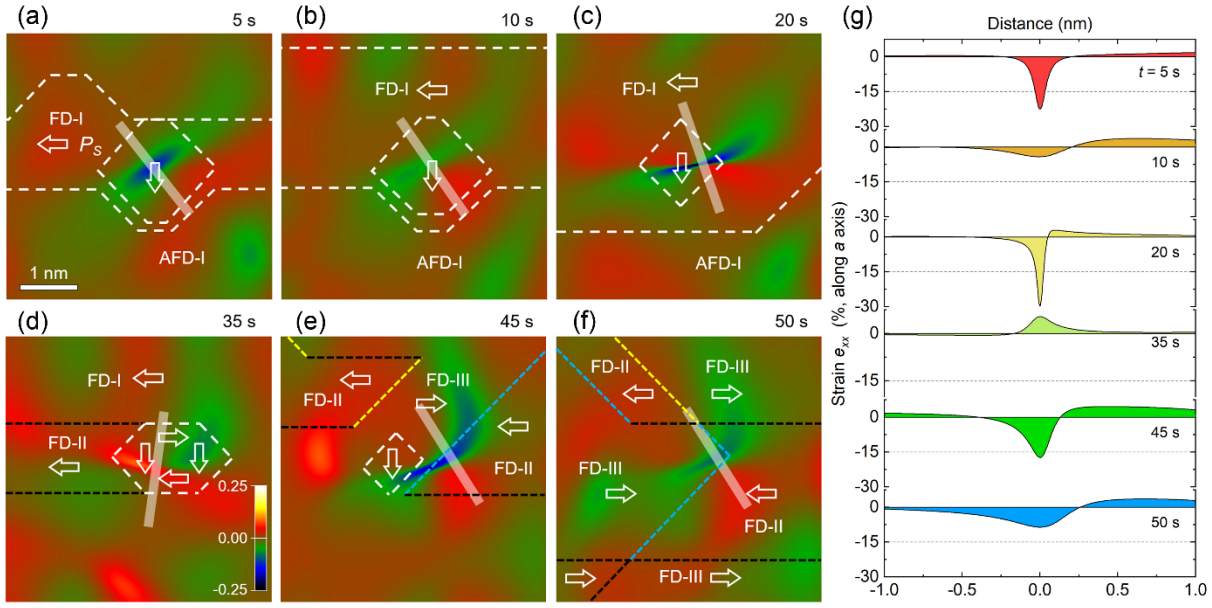

Figure 4. a-f) Maps of e_{xx} lattice strain (along $[100]_O$ direction) obtained from GPA analysis on TEM images shown in Figure 3b-g. The colorful dashed lines denote the phase boundary (white), defect core (white), transversal (black), tail-to-tail (yellow) and head-to-head (blue) charged

domain walls between the ferrodistortive domains, respectively. g) Strain line profiles extracted from the bar-shape regions denoted in the e_{xx} maps shown in (a-f).

Through quantitative measurements and analyses on the atomic-resolution images, we found that the tilting behavior of oxygen octahedra near the defect core is also affected by polarity evolution of the defect core (Figures S8 and S9, Supporting Information). Associated with minimizing the local energy per unit area, the real-time structural changes of nearby regions suggest that the net polarization of the defect core needs to be compensated dynamically. For this reason, the actual size of the defect core becomes variable and extendable, which could be 1 ~ 3 times larger than that delineated in Figure 3. Following the AFD-to-FD transition, further electron-beam irradiation on $PbZrO_3$ instantly transforms the FE/FD phase into the ordinary FE phase.[14]

Together with distribution of the point defects, the shift behavior of oxygen columns relative to centers of the nearest-neighboring Zr columns was mapped and overlaid on the experimental images (**Figure 5**a,b). In the initial ordinary FE state at t = 80 s, we see many FE monoclinic (FE_M) nanodomains, which are characteristic of near $[0\bar{1}0]_O$ polarization orientation. After about one-minute irradiation at t = 135 s, domains with charged configurations are frequently seen at the nanometer scale. As linking to the vacancy distribution, we see that the point defects mainly influence the polarization orientation in the FE_M phase, which is almost ignorable in the FE_R phase. Associated with dynamic transformation between these two phases, the unit-cell-scale FE_R islands are found to embed in the FE_M matrix and grow in size with increase of the irradiation time. This is consistent with proportion change of the FE_M phase ($\phi \approx \pi/2$)[43] and FE_R phase (ϕ = 0) as a function of irradiation time (Figure 5c-f).

Previous studies have reported that the spontaneous polarization is $P_S \approx 32$ and 55 μC cm^{-2} for the FE_M and FE_R phase, respectively.[14,44] This indicates that the FE_M-to-FE_R transition allows further storage of the electrostatic energy by further irradiation of the electron beam, which is accompanied with FE_M domain reorientation and growth of the FE_R domains (Figure S10, Supporting Information). Presence of the high-energy and metastable charged domain walls[45,46] can be understood as a way of temporally storing the injected energy, which may propagate to nearby regions subsequently and the collected charges can be evaluated by $Q(t) = \int_0^t i(t)dt$, i being the stored electric current at a given time t.[47,48] At this stage, the unit-cell-wise FE_M-to-FE_R transition takes place as well (see Figure S11, Supporting Information). Nevertheless, regular domain structure change was not observed due to flexible P_S rotation within certain crystal plane of the FE_M phase,[32] high similarity in lattice parameters[43] and closeness in free energy between these two phases.[49] Relating to the point vacancy distribution, our GPA analysis shows that the initial defect core is dismembered at the ordinary FE states (Figure S12, Supporting Information).

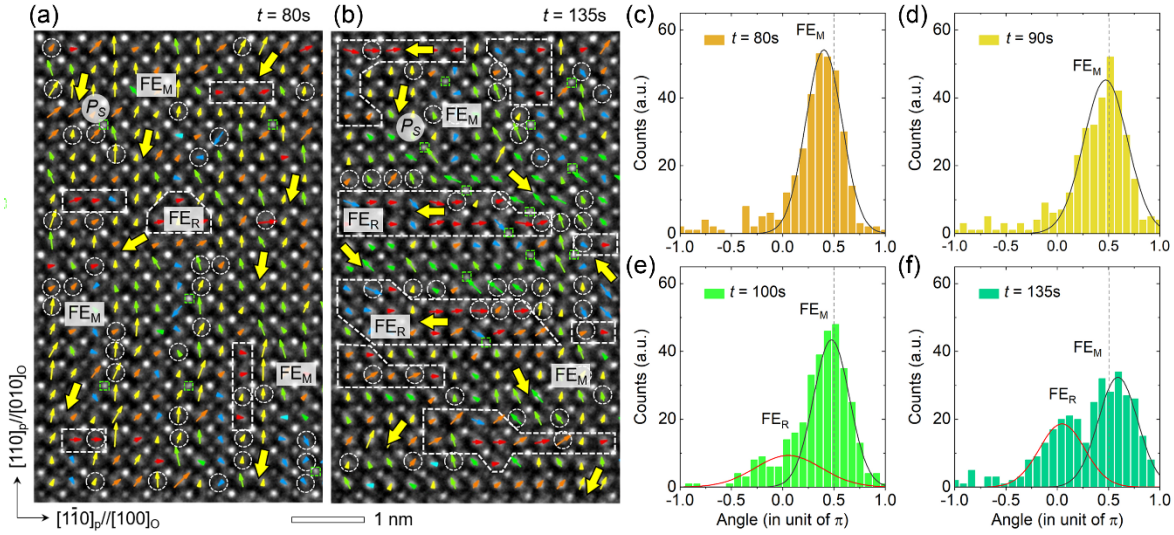

Figure 5. a,b) Atomic-resolution TEM images of ordinary FE phases recorded at t = 80 and 135 s along the $[001]_O$ direction. The oxygen displacement maps (color arrows) against centers of the

nearest-neighboring Zr columns and representative P_S orientation of nanodomains (yellow thick arrows, projected on the $(001)_O$ plane) are overlaid on the images. The white dashed polygons denote the FE_R islands against the FE_M matrix. The white dashed circles and green dashed squares denote oxygen and Pb columns with certain concentration of point vacancy. c-f) Statistical angle analysis of oxygen displacements as a function of electron-beam irradiation time. The angles for the FE_M phase and FE_R phase are at $\phi \approx \pi/2$ and $\phi = 0$, respectively.

As for the driving force of the phase transitions, the following facts suggest that this is dominated by charging effect combined with kinetic energy transfer of the electron beam. For the charging effect, a direct evidence is random shaking of the specimen under electron-beam irradiation inside the microscope, which plays a key role in triggering the step-wise AFD-to-FD transition (Figure S12, Supporting Information). Although occurrence of the phase transition is accompanied with negative electrocaloric effect,[50] a nearly constant magnitude of the Pb-atom antiparallel displacement, in the range of 18 ~ 20 pm, and the shrinking tendency of unit cell volume with time indicate that the contribution of heating effect is ignorable, which leads to gradual decrease of Pb displacement with increasing temperature.[51] With weakening of the charging effect, the kinetic energy transfer through inelastic scattering of electrons drives the subsequent phase transitions in the specimen. This is manifested by the dramatic increase of polarization during the FD-to-ordinary FE state transition.

Regarding the structural phases observed in $PbZrO_3$, the soft-mode theory of phase transition gives a clear classification and interpretation.[52] Usually, the AFD order arises from a mode condensation at the Brillouin zone boundary and leads to unit-cell doubling. As it couples with a polar mode with null polarization, an AFE order emerges in the orthorhombic phase. Instead,

the FD order is triggered by condensation of a zone-center soft mode. In this sense, the AFE and FE transitions are subgroups of AFD and FD transitions, respectively. Nevertheless, the AFD order may also couple with a net polarization, e.g., in the FE_R (*R3c*) phase with $a^-a^-a^-$-type octahedral rotations. For the FE_M (*Cm*) phase with $a^0a^0a^0$-type rotations,[43] there is only zone-center mode condensation. As for the effect of point defects, one can see that it breaks local crystallographic symmetry and introduces local chemical pressure and local polarization, as reported in HfO_2.[53,54] Relative to the capacitor geometry, despite different driving forces, the phase-transition mechanisms[4,5] are expected to be similar given the pinning effect of structural defects and interfaces to electric polarization.[18,19] In addition, the increase of P_r induced by neutron irradiation dose in $PbZrO_3$ suggests that the mechanism reported here may extend to bulk ceramics.[12,55]

3. Conclusions

In summary, benefit from slowing down the energy storage process using electron beam irradiation, our in-situ atomic-resolution TEM study reveals that the point defects play as seeds to initiate the AFE/AFD-to-FE/FD transition. Starting from the vacancy-induced defect core, featured by local compressive strain and polar instability, the AFE/AFD state is step-wisely transformed into the FE/FD state via generation of domain stripes with variable width at unit-cell scale. Specifically, we found formation of charged domain walls at different FE states, which reflects the way of temporally storing injected energy before spreading to nearby regions. Given that proper defect concentration may improve the breakdown electric field and thus U_e,[12,24] it is believed that our findings offer insights to optimize performances, and open up a pathway to configure atomic-scale structure-property relationship in chemical defect-engineered energy storage dielectrics.

4. Experimental Section

Material preparation: The $PbZrO_3$ single crystals were grown by flux method with the PbO-B_2O_3 mixture (soaking at 1,300 K) used as a solvent. Details about the cooling procedures and removal of the residuals were presented elsewhere.[18] The lamella specimens were prepared using an FEI Helios Nanolab 400s focused ion beam system. After removal of the contamination and damaged layers using NanoMill Model 1040 system, which is operated at 500 V, the lamella samples were heated above T_C and then cooled down to room temperature at a rate of ~ 9 K min^{-1}. By repeating this procedure several times, the point vacancy defects are introduced into the lamella specimens.

Imaging experiments: The domain structure analysis and selected-area electron diffraction experiments were carried out on an FEI Tecnai F20 microscope. The atomic resolution TEM experiments were performed on an FEI Titan 80-300 microscope, which is equipped with a *Cs* corrector for the objective lens and is operated at an accelerating voltage of 300 kV. The available point resolution was better than 80 pm and a dose rate of the electron beam was ~ 3.8×10^6 $e.nm^{-2}.s^{-1}$. A 2k × 2k Gatan UltraScan 1000 CCD camera was used for the image acquisition and each frame exposure time was 0.8 s. Structure modelling and multislice-based image simulation were carried out using the CrystalKit-MacTempas software package. The parameters used for simulating the images are C_S = -12 μm, *A1* = 2.5 nm, *A2* = 3 nm, *B2* = 3 nm. The lattice parameters of the image area are measured and averaged by mapping positions of the Zr columns.

Image measurement and quantification: In our experiments, the quantitative measurement and analysis are carried out on as-obtained high quality TEM images, in which the atomic column peak intensities are fitted by 2D Gaussian function based on maximum-likelihood estimation.[35]

Since the antiparallel Pb displacements are compensated in the AFE/AFD and FE/FD phases,[14] the centrosymmetric lattice origin is defined by symmetrizing Pb displacements along the x/$[100]_O$ and y/$[010]_O$ direction.

Supplemental Information

Supplemental Information can be found online.

Acknowledgements

X.-K. Wei acknowledges support by the Deutsche Forschungsgemeinschaft (DFG; German Research Foundation) under Germany's Excellence Strategy - Cluster of Excellence Matter and Light for Quantum Computing (ML4Q) EXC 2004/1-390534769. The authors thank D. Meertens for sample preparation.

Conflict of Interest

The authors declare no competing interests.

Keywords

Energy storage, $PbZrO_3$, in-situ transmission electron microscopy, charged domain walls, ferrodistortive

References

[1] H. Palneedi, M. Peddigari, G.-T. Hwang, D.-Y. Jeong, J. Ryu, *Adv. Funct. Mater.* **2018**, 28, 1803665.

[2] H. Pan, F. Li, Y. Liu, Q. W. Zhang, Meng , S. Lan, Y. Zheng, J. Ma, L. Gu, Y. Shen, P. Yu, S. Zhang, L.-Q. Chen, Y.-H. Lin, C.-W. Nan, *Science* **2019**, *365*, 578.

[3] J. Li, Z. Shen, X. Chen, S. Yang, W. Zhou, M. Wang, L. Wang, Q. Kou, Y. Liu, Q. Li, Z. Xu, Y. Chang, S. Zhang, F. Li, *Nat. Mater.* **2020**, *19*, 999.

[4] B. Xu, J. Iniguez, L. Bellaiche, *Nat. Commun.* **2017**, *8*, 15682.

[5] S. Lisenkov, Y. Yao, N. Bassiri-Gharb, I. Ponomareva, *Phys. Rev. B* **2020**, *102*, 104101.

[6] C. T. Blue, J. C. Hicks, S. E. Park, S. Yoshikawa, L. E. Cross, *Appl. Phys. Lett.* **1996**, 68, 2942.

[7] Y. Cai, F. Phillipp, A. Zimmermann, L. Zhou, F. Aldinger, M. Rühle, Acta Materialia 2003, 51, 6429.

[8] H. He, X. Tan, *Phys. Rev. B* **2005**, *72*, 024102.

[9] B. Chu, X. Zhou, K. Ren, B. Neese, M. Lin, Q. Wang, F. Bauer, Q. M. Zhang, *Science* **2006**, *313*, 334.

[10] X. Tan, C. Ma, J. Frederick, S. Beckman, *J. Am. Ceram. Soc.* **2011**, *94*, 4091.

[11] H. Wang, Y. Liu, T. Yang, S. Zhang, *Adv. Funct. Mater.* **2019**, *29*, 1807321.

[12] X. Liu, Y. Li, N. Sun, X. Hao, *Inorg. Chem. Front.* **2020**, *7*, 756.

[13] T. Zhang, Y. Zhao, W. Li, W. Fei, *Energy Storage Mater.* **2019**, *18*, 238.

[14] X. K. Wei, C. L. Jia, H. C. Du, K. Roleder, J. Mayer, R. E. Dunin-Borkowski, *Adv. Mater.* **2020**, *32*, 1907208.

[15] H. Zheng, J. B. Rivest, T. A. Miller, B. Sadtler, A. Lindenberg, M. F. Toney, L.-W. Wang, C. Kisielowski, A. P. Alivisatos, *Science* **2011**, *333*, 206.

[16] B. K. Mani, C. M. Chang, S. Lisenkov, I. Ponomareva, *Phys. Rev. Lett.* **2015**, *115*, 097601.

[17] C. L. Jia, L. Houben, A. Thust, J. Barthel, *Ultramicroscopy* **2010**, *110*, 500.

[18] X.-K. Wei, A. K. Tagantsev, A. Kvasov, K. Roleder, C.-L. Jia, N. Setter, *Nat. Commun.* **2014**, *5*, 3031.

[19] X.-K. Wei, Y. Yang, L. J. McGilly, L. Feigl, R. E. Dunin-Borkowski, C.-L. Jia, L. Bellaiche, N. Setter, *Phys. Rev. B* **2018**, *98*, 020102(R).

[20] X. Hao, J. Zhai, L. B. Kong, Z. Xu, *Prog. Mater. Sci.* **2014**, *63*, 1.

[21] T. Ma, Z. Fan, B. Xu, T.-H. Kim, P. Lu, L. Bellaiche, M. J. Kramer, X. Tan, L. Zhou, *Phys. Rev. Lett.* **2019**, *123*, 217602.

[22] Z. Fu, X. Chen, Z. Li, T. Hu, L. Zhang, P. Lu, S. Zhang, G. Wang, X. Dong, F. Xu, *Nat. Commun.* **2020**, *11*, 3809.

[23] S. Li, H. Nie, G. Wang, C. Xu, N. Liu, M. Zhou, F. Cao, X. Dong, *J. Mater. Chem. C* **2019**, *7*, 1551.

[24] N. Luo, K. Han, F. Zhuo, C. Xu, G. Zhang, L. Liu, X. Chen, C. Hu, H. Zhou, Y. Wei, *J. Mater. Chem. A* **2019**, *7*, 14118.

[25] H. Qi, R. Zuo, A. Xie, A. Tian, J. Fu, Y. Zhang, S. Zhang, *Adv. Funct. Mater.* **2019**, *29*, 1903877.

[26] K. Roleder, J. Dec, *J. Phys.: Condens. Matter.* **1989**, *1*, 1503.

[27] X.-K. Wei, C.-L. Jia, K. Roleder, N. Setter, *Mater. Res. Bull.* **2015**, *62*, 101.

[28] X.-K. Wei, K. Vaideeswaran, C. S. Sandu, C.-L. Jia, N. Setter, *Adv. Mater. Interfaces* **2015**, *2*, 1500349.

[29] V. I. Arkhipox, A. I. Rudenko, G. M. Sessier, *J. Phys. D: Appl. Phys.* **1993**, *26*, 1298.

[30] R. F. Egerton, P. Li, M. Malac, *Micron* **2004**, *35*, 399.

[31] C. L. Jia, M. Lentzen, K. Urban, *Science* **2003**, *299*, 870.

[32] X.-K. Wei, C.-L. Jia, T. Sluka, B.-X. Wang, Z.-G. Ye, N. Setter, *Nat. Commun.* **2016**, *7*, 12385.

[33] D. L. Corker, A. M. Glazer, J. Dec, K. Roleder, R. W. Whatmore, *Acta Cryst. B* **1997**, *53*, 135.

[34] K. Yamasaki, Y. Soejima, K. F. Fischer, *Acta Cryst. B* **1998**, *54*, 524-530.

[35] R. Parthasarathy, *Nat. Methods* **2012**, *9*, 724.

[36] V. Stepkova, P. Marton, N. Setter, J. Hlinka, *Phys. Rev. B* **2014**, *89*, 060101.

[37] Y. Nahas, S. Prokhorenko, L. Bellaiche, *Phys. Rev. Lett.* **2016**, *116*, 117603.

[38] M. J. Hÿtch, E. Snoeck, R. Kilaas, *Ultramicroscopy* **1998**, *74*, 131.

[39] T. Qi, I. Grinberg, A. M. Rappe, *Phys. Rev. B* **2010**, *82*, 134113.

[40] C. L. Jia, S. B. Mi, K. Urban, I. Vrejoiu, M. Alexe, and D. Hesse, *Nat. Mater.* **2008**, *7*, 57.

[41] S. E. Reyes-Lillo, K. M. Rabe, *Phys. Rev. B* **2013**, *88*, 180102.

[42] H. Fujishita, Y. Shiozaki, and E. Sawaguchi, *J. Phys. Soc. Jpn.* **1979**, *46*, 1391.

[43] H. Yokota, N. Zhang, A. E. Taylor, P. A. Thomas, and A. M. Glazer, Phys. Rev. B 2009, *80* 104109.

[44] R. Kagimura, D. Singh, *Phys. Rev. B* **2008**, *77*, 104113.

[45] T. Sluka, A. K. Tagantsev, P. Bednyakov, N. Setter, *Nat. Commun.* **2013**, *4*, 1808.

[46] X. K. Wei, T. Sluka, B. Fraygola, L. Feigl, H. Du, L. Jin, C. L. Jia, N. Setter, *ACS Appl. Mater. Interfaces* **2017**, *9*, 6539−6546.

[47] A. I. Khan, K. Chatterjee, B. Wang, S. Drapcho, L. You, C. Serrao, S. R. Bakaul, R. Ramesh, S. Salahuddin, *Nat. Mater.* **2015**, *14*, 182.

[48] P. Maksymovych, S. Jesse, P. Yu, R. Ramesh, A. P. Baddorf, S. V. Kalinin, *Science* **2009**, *324*, 1421.

[49] J. A. Rodriguez, A. Etxeberria, L. Gonzalez, and A. Maiti, *J. Chem. Phys.* **2002,** *117*, 2699.

[50] P. Vales-Castro, R. Faye, M. Vellvehi, Y. Nouchokgwe, X. Perpinà, J. M. Caicedo, X. Jordà, K. Roleder, D. Kajewski, A. Perez-Tomas, E. Defay, G. Catalan, arXiv:2009.02184 2020.

[51] R. W. Whatmore, A. M. Glazer, *J. Phys. C: Solid State Phys.* **1979**, *12*, 1505

[52] M. E. Lines, A. M. Glass, *Principles and Applications of Ferroelectrics and Related Materials*. *Oxford Univ. Press* (2001).

[53] X. Sang, E. D. Grimley, T. Schenk, U. Schroeder, J. M. LeBeau, *Appl. Phys. Lett.* 2015, 106, 162905.

[54] M. D. Glinchuk, A. N. Morozovska, A. Lukowiak, W. Stręk, M. V. Silibin, D. V. Karpinsky, Y. Kim, S. V. Kalinin, *J. Alloy Compd.* **2020**, *830*, 153628.

[55] R. Bittner, K. Humer, H. W. Weber, K. Kundzins, A. Sternberg, D. A. Lesnyh, D. V. Kulikov, Y. V. Trushin, *J. Appl. Phys.* **2004**, *96*, 3239.

TOC figure

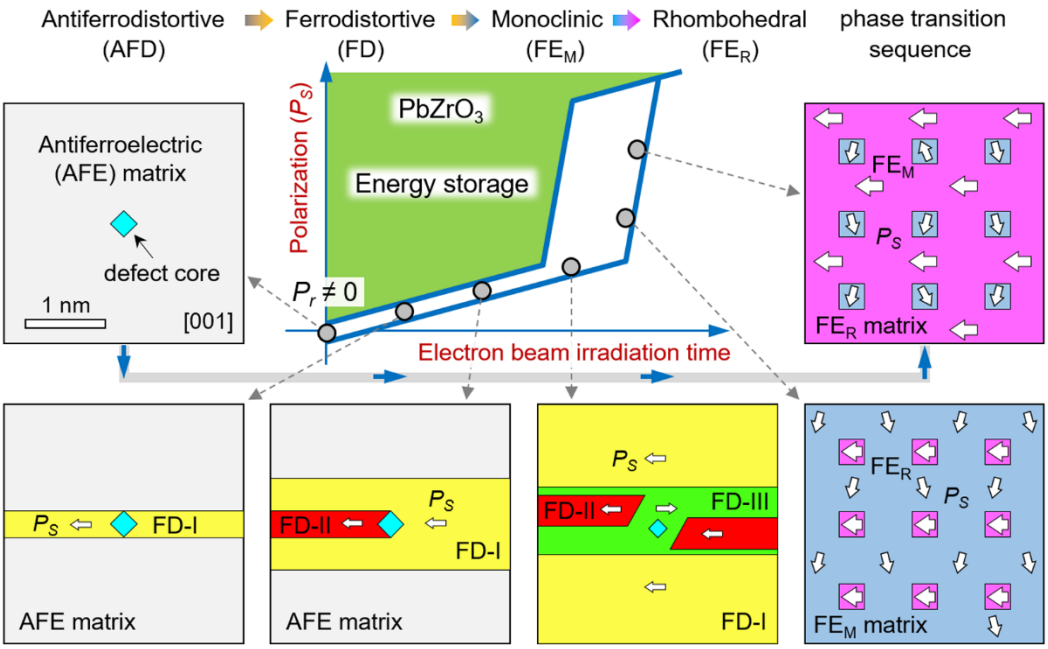

In-situ probing the energy storage pathway provides a fundamental perspective to elaborate the structure-property relationship. Here, by slowing down the phase-transition speed, our in-situ atomic-scale transmission electron microscopy study on antiferroelectric $PbZrO_3$ reveals that associated with presence of charged domain walls, point defects may act as seeds to initiate the unit-cell-wise structural phase transition and electrostatic energy storage.

Supporting Information

In-situ Observation of Point-Defect-Induced Unit-Cell-Wise Energy Storage Pathway in Antiferroelectric $PbZrO_3$

Xian-Kui Wei, Chun-Lin Jia, Krystian Roleder, Rafal E. Dunin-Borkowski, and Joachim Mayer*

*Corresponding author E-mail: x.wei@fz-juelich.de

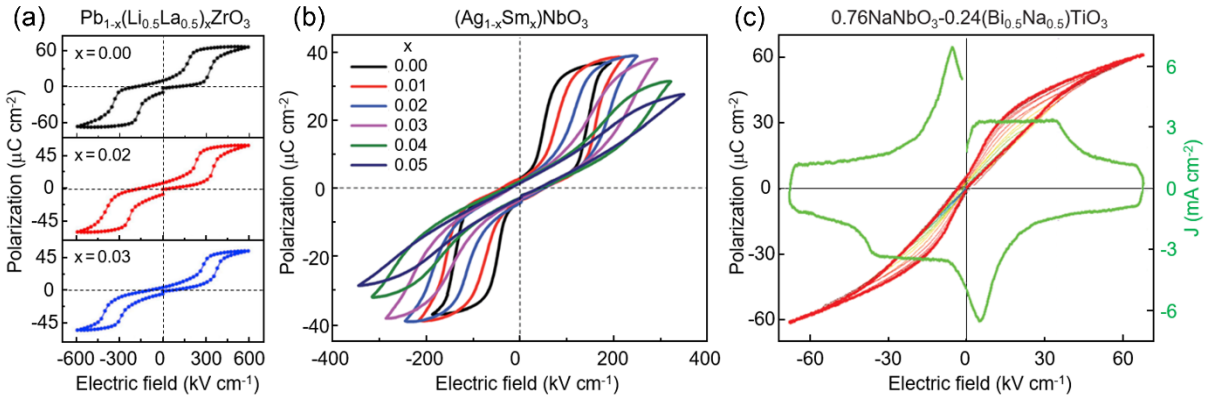

Figure S1. Remnant polarization in typical antiferroelectric materials. a) Polarization-electric field (*P*-*E*) hysteresis loops of AFE $Pb_{1-x}(Li_{0.5}La_{0.5})_xZrO_3$ with x = 0.00, 0.02 and 0.03.[12] The remnant polarization is in the range of P_r = 3.5 ~ 8.3 μC cm^{-2}. b) The *P*-*E* hysteresis loops of AFE $(Ag_{1-x}Sm_x)NbO_3$ with x = 0.00, 0.01, 0.02, 0.03, 0.04 and 0.05.[24] The remnant polarization is $P_r \approx 2.8$ μC cm^{-2}. c) The *P*-*E* hysteresis loops under different electric fields and current-*E* curve of $0.76NaNbO_3$-$0.24(Bi_{0.5}Na_{0.5})TiO_3$ relaxor AFE measured at a frequency of 10 Hz.[25] The remnant polarization is $P_r \approx 2.5$ μC cm^{-2}.

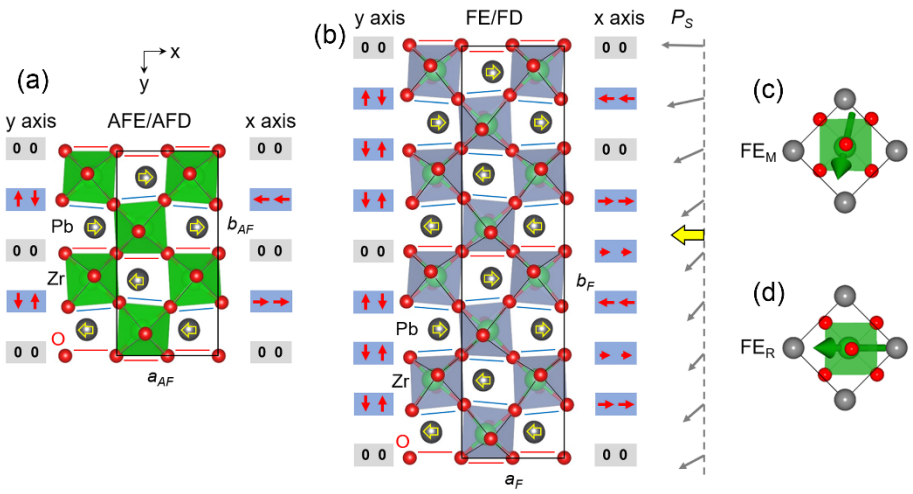

Figure S2. Structure and polarization feature of AFE/AFD, FE/FD, FE_M and FE_R phase of $PbZrO_3$. a,b) Crystal structure of AFE-AFD phase and FE-FD phase of $PbZrO_3$ viewed along the $[001]_O$ direction, respectively. The Pb atoms with antiparallel displacements are denoted by empty yellow arrows. The red arrows and blue line segments denote the characteristic displacements of oxygen along x and y direction. The zeros "0" and red line segments denote the oxygen atoms locating at the centrosymmetric positions. The x-direction oxygen shift induced unit-cell doubling can be identified from the FE/FD phase shown in (b), which is characteristic of the cycloidal polarization order (grey arrows on the right)[14] with P_S essentially running along the x direction. c,d) Schematic unit cell of the ferroelectric monoclinic (FE_M) and rhombohedral (FE_R) phase, respectively. The P_S in the FE_M phase is flexibly rotatable within the pseudocubic $(110)_p$ crystal plane.

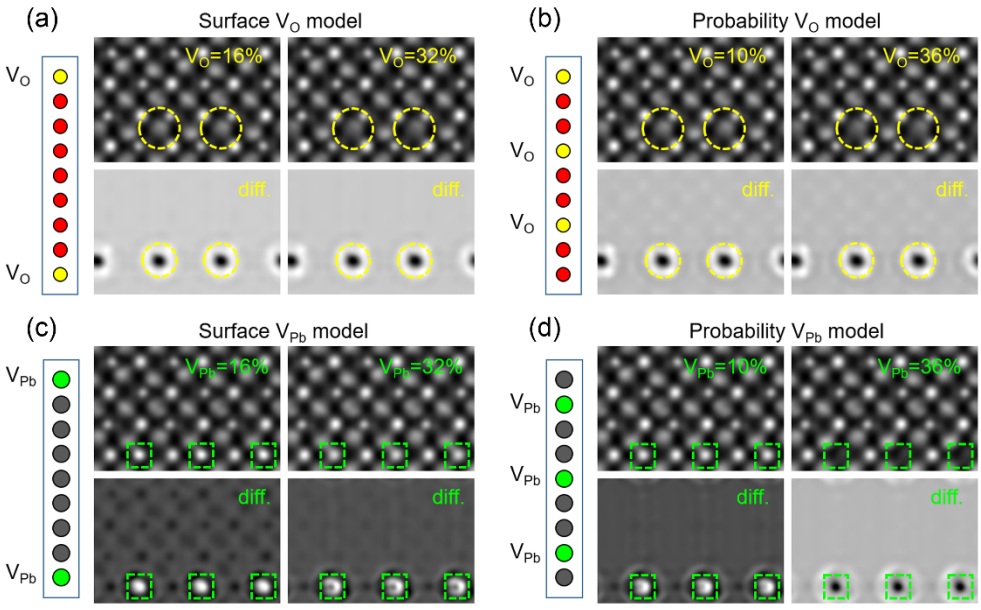

Figure S3. Image simulation based on different vacancy models. a,c) Surface vacancy models with vacancy content of V_O and V_{Pb} at 16% and 32% for the specific column, respectively. b,d) Probability vacancy models with vacancy content of V_O and V_{Pb} at 10% and 36% for the specific column, respectively. With respect to the V_{Pb} = 10% condition, we see the contrast reduction as the V_{Pb} concentration increases to 36% at this specific atomic column. The differences of the vacancy-containing simulated images with the vacancy-free simulated ones are illustrated at the bottom rows. The images are simulated at a specimen thickness of 10.2 nm and a defocus value of 8.5 nm based on the multi-slice method.

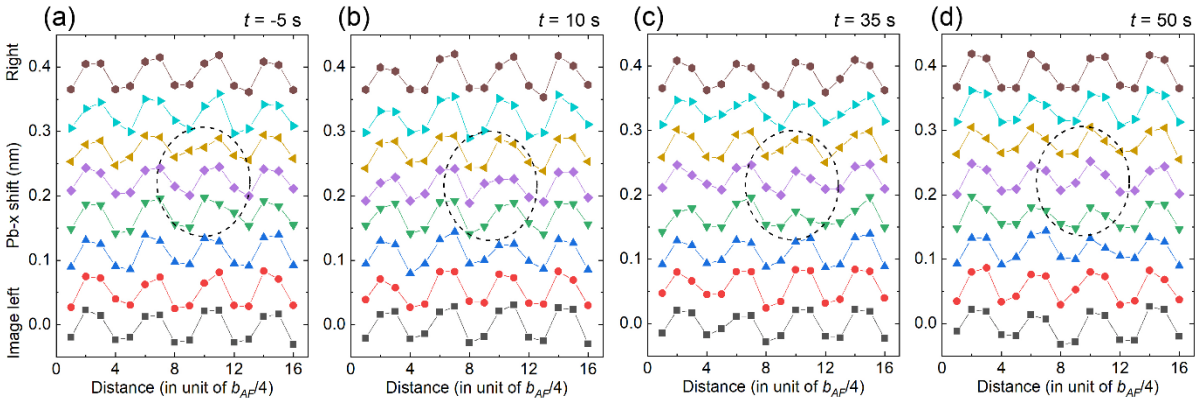

Figure S4. Evolution of antiparallel Pb shifts near the defect core as a function of electron-beam irradiation. a-d) Antiparallel Pb displacements along $[100]_O$ direction plotted as a function of distance along $[010]_O$ direction at irradiation time t = -5, 10, 35 and 50 s, respectively. These plots correspond to atomic-resolution TEM images shown in Figure 2a,c,e and g, respectively. With respect to the TEM images, the plots shown here are anticlockwise rotated by 90 degree. The dashed black circles denote positions of the defect core, where deviation from the regular Pb shifts can be seen at specific atomic sites.

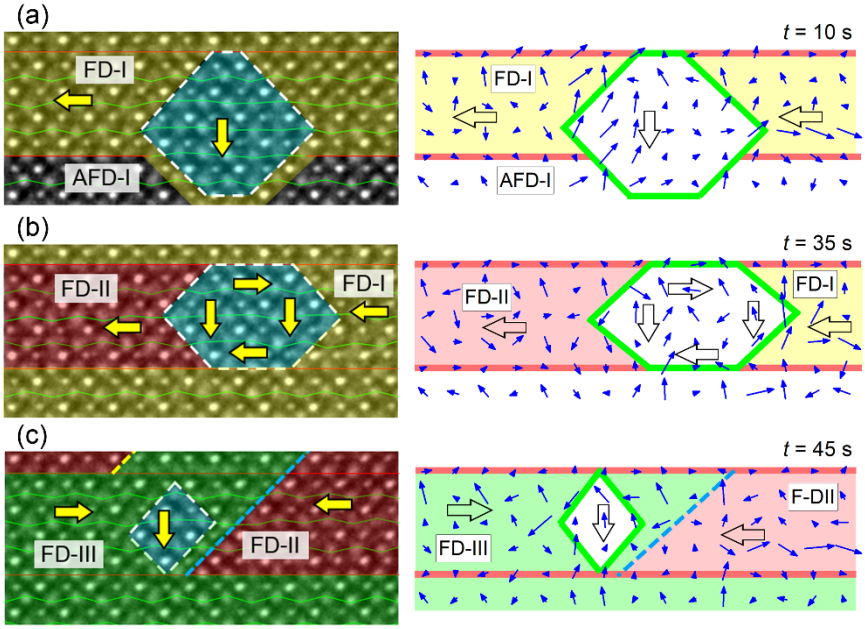

Figure S5. Determination of oxygen polar displacements near the defect core and nearby domains. a-c) The atomic-resolution TEM images near the defect core with recording time at t = 10, 35 and 50 s, annotation of the AFD, FD (yellow, red and green shadows) domain states and orientation of spontaneous polarization derived from mapping of oxygen shifts with respect to centers of the nearest-neighboring Zr columns. The red (thin and thick) and green solid lines denote the shifts of oxygen along y direction. The dashed yellow and blue lines denote the tail-to-tail and head-to-head charged domain walls.

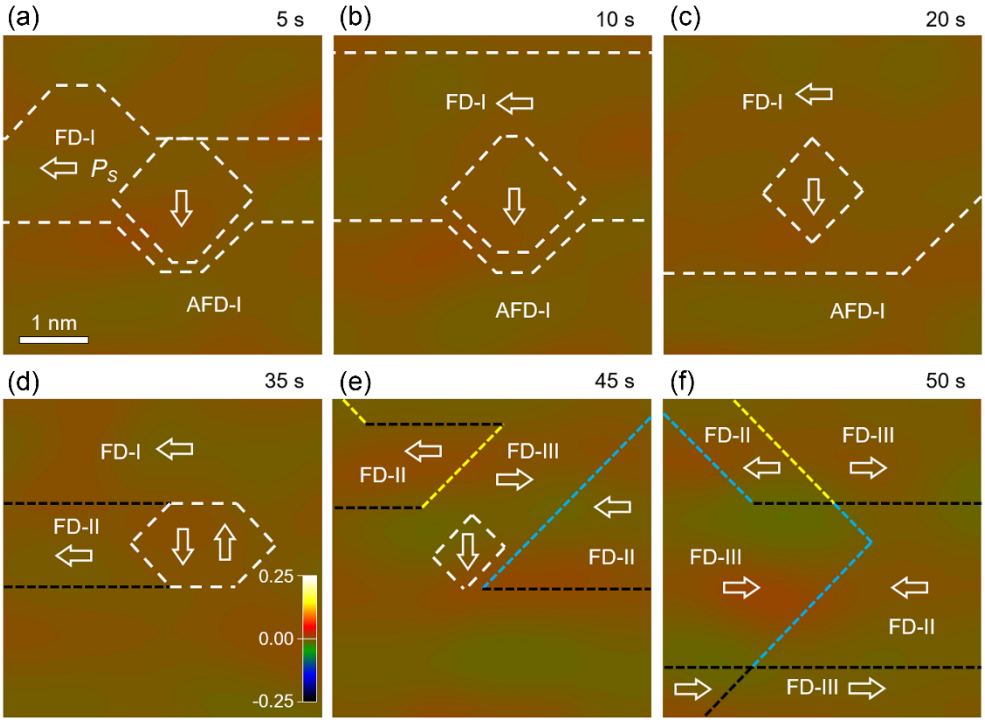

Figure S6. Evolution of lattice strain (e_{yy}) map as a function of electron-beam irradiation time from GPA analysis. a-f) The e_{yy} map (along $[010]_O$ direction) for TEM images recorded at t = 5, 10, 20, 35, 45 and 50 s, respectively. The colorful dashed lines denote the phase boundary (white), defect core (white), transversal (black), tail-to-tail (yellow) and head-to-head (blue) charged domain walls between the ferrodistortive domains, respectively.

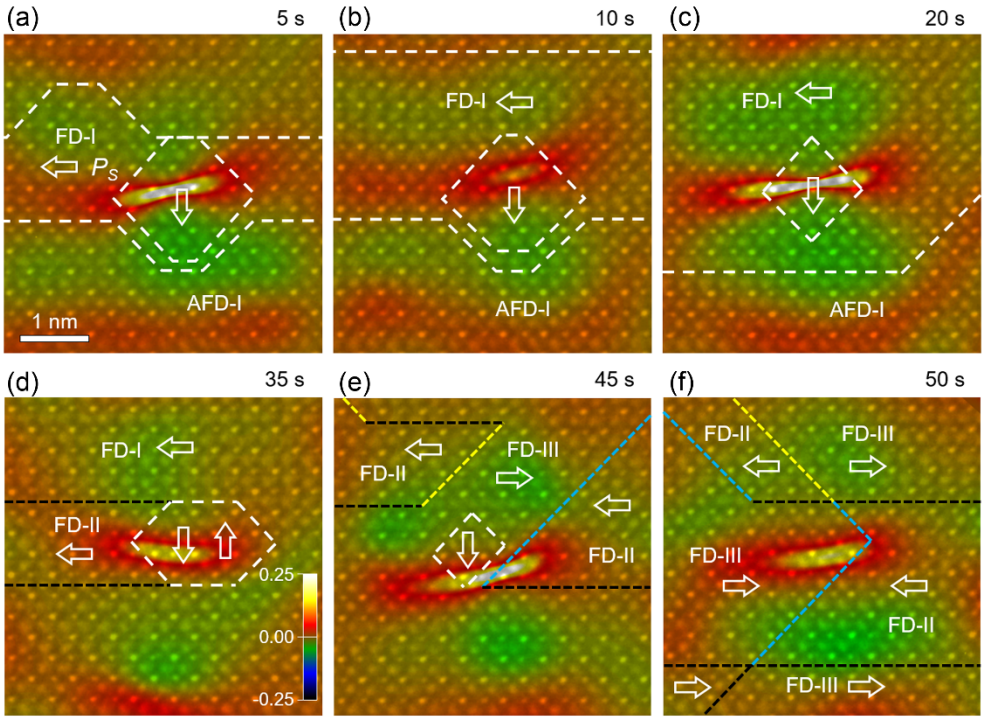

Figure S7. Evolution of lattice rotation (rot_{xy}) map as a function of electron-beam irradiation time from GPA analysis. a-f) The rot_{xy} map for TEM images recorded at t = 5, 10, 20, 35, 45 and 50 s, respectively. The shear strain e_{xy} map shows almost the same behavior as the rot_{xy} map. The colorful dashed lines denote the phase boundary (white), defect core (white), transversal (black), tail-to-tail (yellow) and head-to-head (blue) charged domain walls between the ferrodistortive domains, respectively. Accompanied with presence and growth of the FD domains, dynamic changes of the defect core, e.g., position and length, orientation and local lattice rotation can be clearly seen.

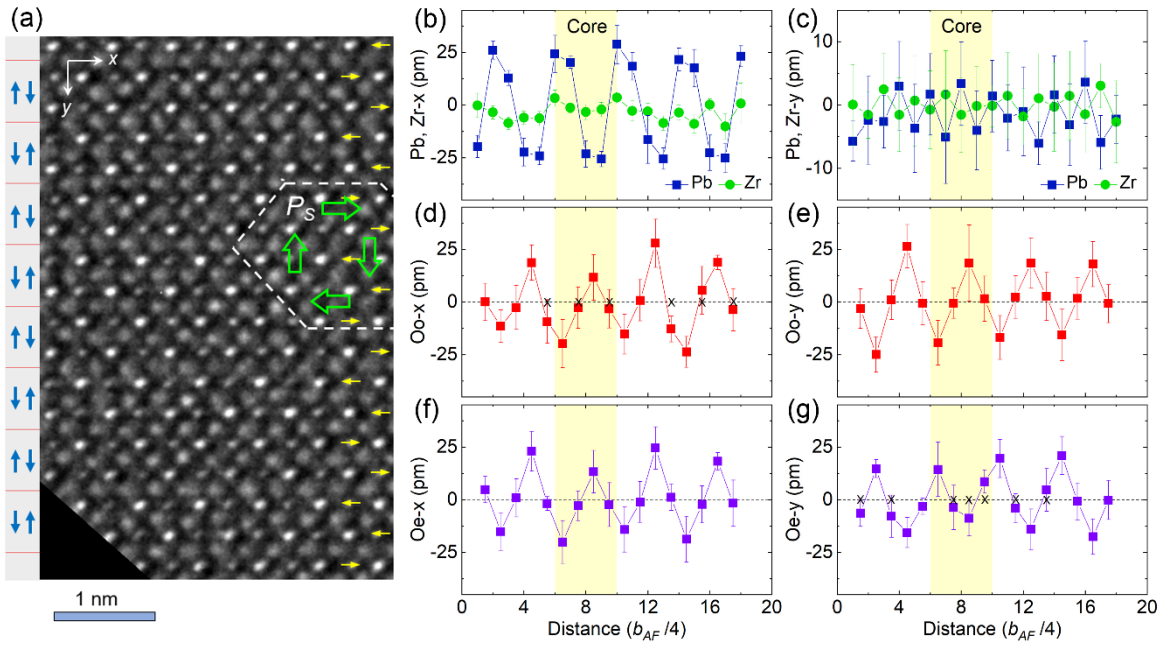

Figure S8. Quantitative analysis on atomic displacements near the defect core for the image recorded at t = -5 s. a) Atomic-resolution TEM image of $PbZrO_3$ recorded along $[001]_O$ direction. The yellow arrows and white dashed line denote the antiparallel Pb shifts and the defect core. The red solid lines and blue arrows denote the oxygen atoms locating at the neutral sites and those undergoing the y-direction shifts, respectively. b,c) Atomic displacements of Pb and Zr atoms along the x//[100] and y//[010] direction, respectively. d-g) Atomic displacements of odd-column (Oo) and even-column oxygen (Oe) atoms along the x and y direction, respectively. The presented data profiles are averaged along the x direction.

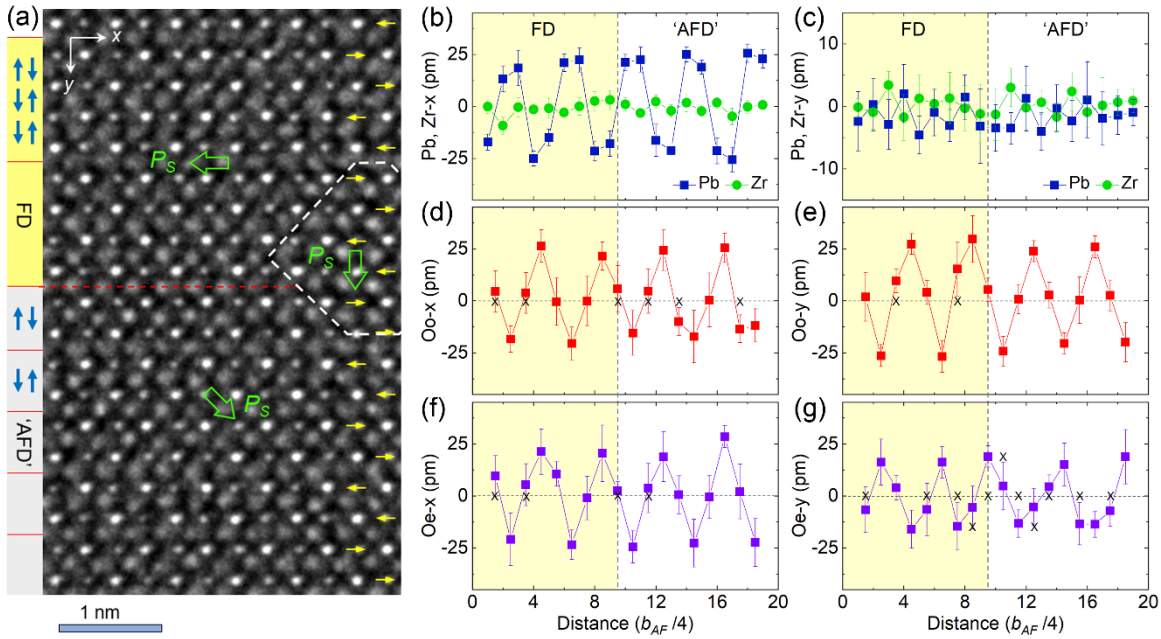

Figure S9. Quantitative analysis on atomic displacements near the defect core for the image recorded at t = 10 s. a) Atomic-resolution TEM image of $PbZrO_3$ recorded along $[001]_O$ direction. The yellow arrows and white dashed line denote the antiparallel Pb shifts and the defect core. The red solid and dashed lines denote the oxygen atoms locating at the neutral sites and the AFD/FD phase boundary, respectively. b,c) Atomic displacements of Pb and Zr atoms along the x//$[100]_O$ and y//$[010]_O$ direction, respectively. d-g) Atomic displacements of Oo and Oe atoms along the x and y direction, respectively. The presented data profiles are averaged along the x direction.

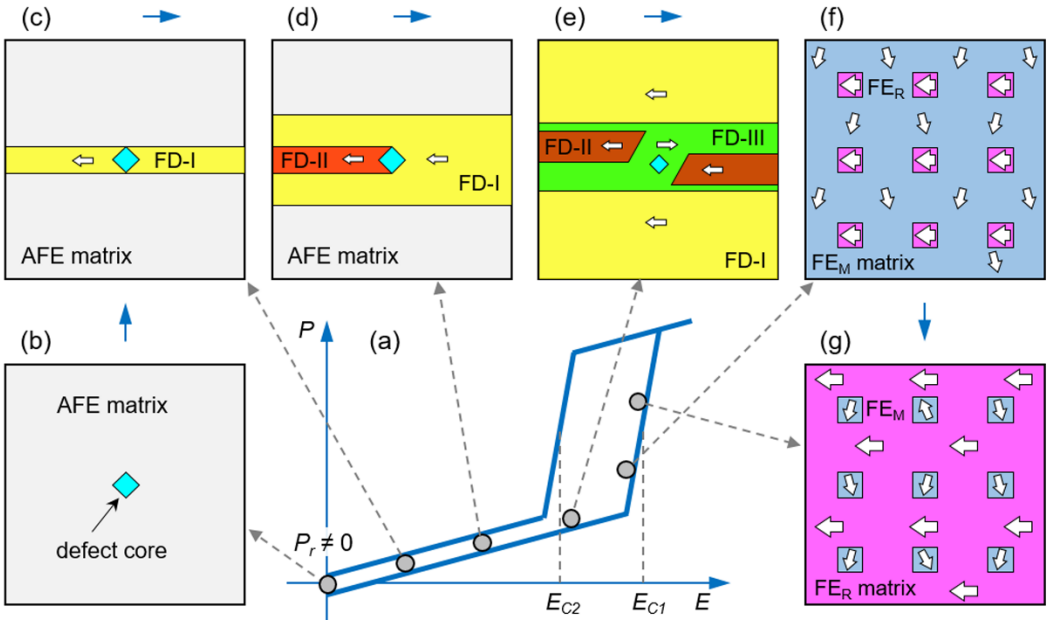

Figure S10. Illustration of energy storage process in $PbZrO_3$ according to experimental observations. a) Schematic hysteresis loop. b-e) Defect core induced AFD-to-FD state transition, growth of FD-I state, generation of FD-II and FD-III states with formation of charged domain walls, respectively. f) FE_M matrix with embedding of FE_R nanoislands. g) FE_R matrix with embedding of FE_M nanoislands. The size of black-stroked white arrows denotes magnitude of the polarization in different FE phases.

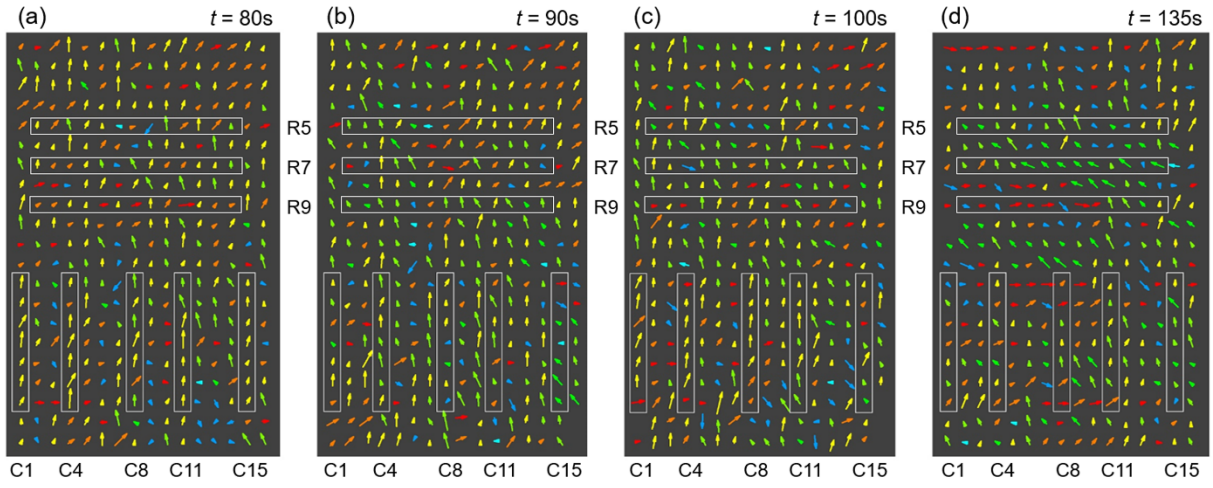

Figure S11. Unit-cell-wise FE_M-to-FE_R transition. a-d) The evolution of oxygen displacements (color arrows) against centers of the nearest-neighboring Zr columns in ordinary FE $PbZrO_3$. To facilitate identifying the unit-cell-wise FE_M-to-FE_R transition, certain atomic columns (C1, C4, C8, C11, C15) and rows (R5, R7, R9) are delineated to track changes of oxygen displacements during the energy-storage process. One can see the unit-cell-wise FE_M-to-FE_R transition, but very regular domain structure change can hardly be identified.

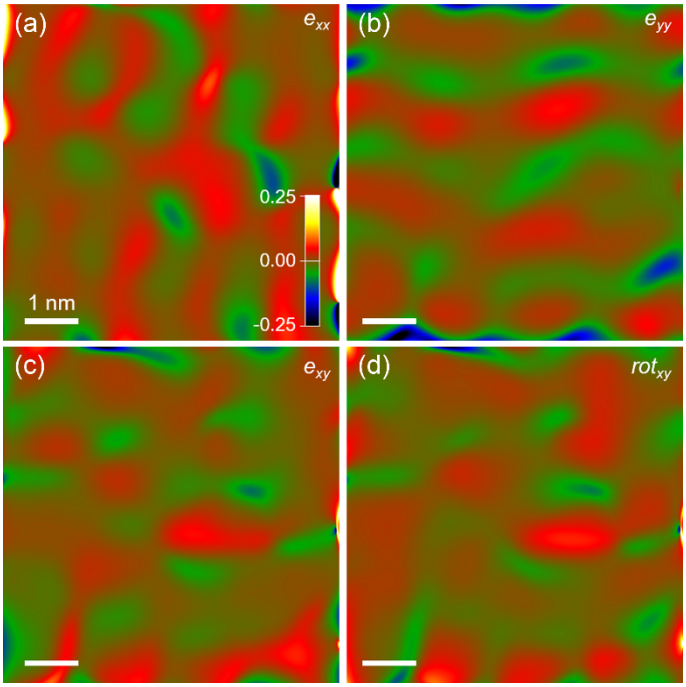

Figure S12. GPA analysis for the FE_M phase recorded at t = 80 s. a-d) The e_{xx}, e_{yy}, e_{xy} and lattice rotation rot_{xy} maps. The x and y directions are selected along $[100]_O$ and $[010]_O$ direction, respectively.

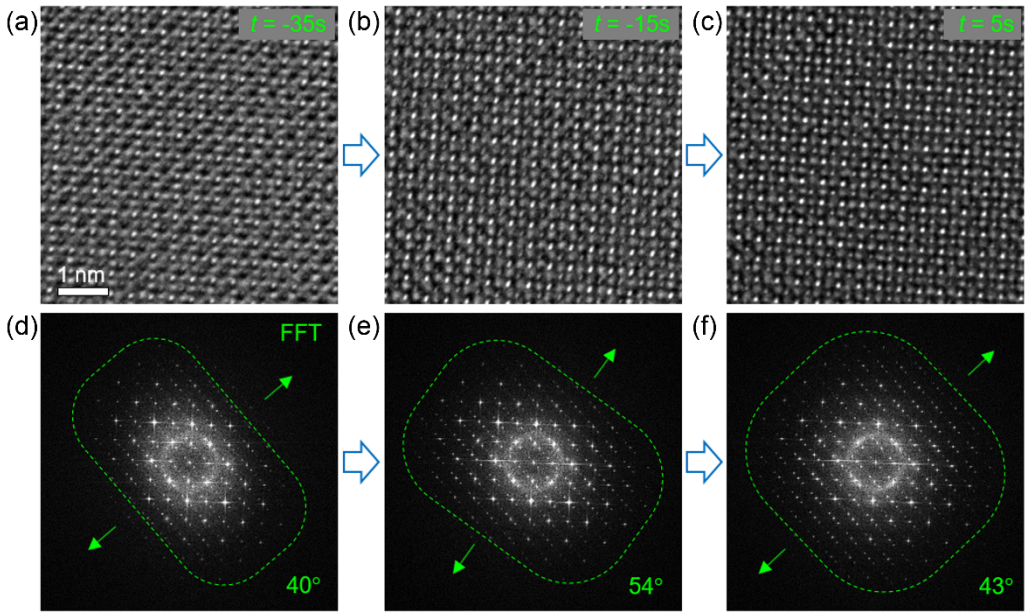

Figure S13. Direct evidence of charging effect of $PbZrO_3$ during irradiation induced energy storage. a-c) Atomic resolution TEM images recorded along the $[001]_O$ direction at t = -35, -15 and 5 s, respectively. d-f) Corresponding fast Fourier transform (FFT) images of (a-c), respectively. The electron beam charging effect leads to cutting of the diffractogram along certain direction. The angles denote the short-axis direction of the green dashed squares, delineating contour of the intensity distribution of diffractogram, away from the horizontal axis.